Transport properties of interface-type analog memristors

Sahitya V. Vegesna *

Department of Quantum Detection, Leibniz Institute of Photonic Technology (IPHT), Albert-Einstein-Straße 9, 07745 Jena, Thuringia, Germany and
Institute for Solid State Physics, Friedrich Schiller University Jena, Helmholtzweg 3, 07743 Jena, Thuringia, Germany

Venkata Rao Rayapati

Department of Quantum Detection, Leibniz Institute of Photonic Technology (IPHT), Albert-Einstein-Straße 9, 07745 Jena, Thuringia, Germany

Heidemarie Schmidt†

Department of Quantum Detection, Leibniz Institute of Photonic Technology (IPHT), Albert-Einstein-Straße 9, 07745 Jena, Thuringia, Germany and
Institute for Solid State Physics, Friedrich Schiller University Jena, Helmholtzweg 3, 07743 Jena, Thuringia, Germany

(Received 13 February 2024; revised 10 June 2024; accepted 15 July 2024; published 12 September 2024)

Interface-type, analog memristors have quite a reputation for real-time applications in edge sensorics, edge computing, and neuromorphic computing. The *n*-type conducting $BiFeO_3$ (BFO) is such an interface-type, analog memristor, which is also nonlinear and can therefore not only store, but also process data in the same memristor cell without data transfer between the data-storage unit and the data-processing unit. Here we present a physical memristor model, which describes the hysteretic current-voltage curves of the BFO memristor in the small and large current-voltage range. Extracted internal state variables are reconfigured by the ion drift in the two write branches and are determining the electron transport in the two read branches. Simulation of electronic circuits with the BFO interface-type, analog memristors was not possible so far because previous physical memristor models have not captured the full range of internal state variables. We show quantitative agreement between modeled and experimental current-voltage curves exemplarily of three different BFO memristors in the small and large current-voltage ranges. Extracted dynamic and static internal state variables in the two full write branches and in the two full read branches, respectively, can be used for simulating electronic circuits with BFO memristors, e.g., in edge sensorics, edge computing, and neuromorphic computing.

DOI: 10.1103/PhysRevApplied.22.034028

I. INTRODUCTION

The advent of the Internet of Things (IoT) has transformed our technologically interconnected society, leading to a surge in the demand for computational resources. This increase in computational needs is intimately linked with a growth in energy consumption, a situation that is becoming increasingly untenable as we approach the limitations defined by Moore's law. Consequently, the pursuit of more efficient computational methodologies has become imperative for the next phase of technological advancement. Research has pointed to innovative pathways such as the development of improved algorithms [1–3] and the exploration of alternative memory elements [4–6] that deviate from conventional semiconductor technology. Such alternative memory elements are one of the core enablers for artificial intelligence (AI) accelerator hardware. AI design needs to handle a lot of design corners, e.g., the development of physical models describing the core enabler hardware. Within this context, memristors have emerged as a promising solution.

Memristors serve as pivotal elements with extensive applicability [7–10] in advancing the domains of AI [11,12], neural networks [13,14], and secure electronics [15,16]. In particular, the bismuth iron oxide $BiFeO_3$ (BFO) has attracted attention as a useful material for interface-type, analog, and nonlinear memristors [17,18].

*Contact author: sahitya.vegesna@uni-jena.de
†Contact author: heidemarie.schmidt@uni-jena.de

Published by the American Physical Society under the terms of the Creative Commons Attribution 4.0 International license. Further distribution of this work must maintain attribution to the author(s) and the published article's title, journal citation, and DOI.

BFO thin films are intrinsically n-type conducting due to the formation of oxygen vacancy donor ions during fabrication. The current-voltage characteristics of BFO thin films with two metallically conducting electrodes may reveal hysteretic behavior. Such BFO-based structures are called BFO memristors. The hysteretic current-voltage characteristics of BFO memristors reveal four current-voltage branches, two full reconfigurable write branches with dynamic internal state variables and two full unaltered read branches with static internal state variables [19]. Oxygen vacancies in BFO thin films with two metallically conducting electrodes only drift between the two metallically conducting electrodes in the two write branches and not in the two read branches in the electric field of the applied voltage [20]. The redistribution of oxygen vacancies in the two write branches can be described by a rigid-point ion model [7]. In BFO memristors, the diffusion of oxygen vacancies due to a chemical or thermal gradient is suppressed by substitutional Ti^{4+} ions trapping the oxygen vacancies. Both the quasi-Fermi-level (E_F (BFO)) and the conduction-band minimum in BFO (E_C) depend on the distribution of the oxygen vacancies and determine the internal-state variables of the BFO memristor. Because the distribution of oxygen vacancies does not change in the two read branches, the internal-state variables in the two read branches are unaltered and static. Because the distribution of oxygen vacancies changes in the two write branches, the internal-state variables in the two write branches are reconfigurable and dynamic. Whether the BFO memristor is operated in the read or in the write mode solely depends on whether the oxygen-vacancy distribution in the BFO memristor remains unchanged or is continuously changed, respectively. BFO memristors show a changing memristance in the two full-write branches and no change of memristance in the two full-read branches [21]. Furthermore, due to the nonlinear current voltage curves, the resistance of the BFO memristor is continuously changed in the two full-read branches. Self-rectification characteristics are often observed in memristors with reconfigurable Schottky barrier, which appear in both measured and modeled data, but the corresponding analysis is inadequate [22,23]. For example, the study by Chen *et al*. [22] models experimental hysteretic current-voltage curves of BFO memristors only adequately at large voltages. And the study by Yarragolla *et al*. [23] models hysteretic current-voltage curves of BFO memristors adequately at small and large voltages, but assumes a change of Schottky barrier not only in the two full-write branches but also in the two full-read branches. This results in inconsistencies pertaining to the reconfiguration of the quasi-Fermi-level and to the modulation of the Schottky-barrier height of the two metallically conducting electrodes attached to the BFO memristor. The model presented here correctly describes that the Schottky-barrier height can be reconfigured only in the two full-write branches and not in the two full-read branches. For advancing the development of electronic circuits with BFO memristors a clear understanding of the dependence of internal-state parameters on the operation of BFO memristors is necessary [24]. The physical memristor model of hysteretic current-voltage curves of interface-type memristors has to account for the dominating ion drift in the two write branches and its influence on the internal-state variables, which determine the electron drift in the two read branches. Such a model will pave the way for alternative electrical and electronic devices with BFO memristors that merge data processing and storage in the same device cell, essentially combining memory and processing without data transfer between memory and processor. Building on this, we propose a physical memristor model where the internal-state variables change only in the two complete write branches, leaving the read branches unaffected. This approach accurately reproduces the hysteretic I-V characteristics of n-type conducting, interface-type memristors in both small and large bias ranges and aligns the tendencies of the reconfigurable Schottky-barrier height with theoretical band-alignment predictions.

Figure 1 offers an insightful perspective into the read and write operation of BFO memristors. BFO is a multiferroic material with ferroelectric ordering (ferroelectric Curie temperature $T_c = 1083$ K [25]) and antiferromagnetic ordering (antiferromagnetic Néel temperature $T_N = 643$ K [26]). When a voltage is sourced to operate the BFO memristor below the ferroelectric Néel temperature, spontaneous electric polarization can be reversed and a polarization switching current flows [27]. Resistive switching in BFO thin films with a metallically conducting bottom electrode and a metallically conducting top electrode has been reported and attributed to ferroelectric polarization current [17,28]. We observed another type of resistive switching in BFO thin films and attributed it to a reconfigurable Schottky barrier height of the electrodes [7,29]. In this work, we focus on analyzing the hysteretic current-voltage curves of BFO thin films revealing exclusively resistive switching due to reconfigurable Schottky barrier heights of the electrodes and revealing no ferroelectric switching. We call BFO memristors with such a hysteretic current-voltage curve "memristors with an ideal current" response [Fig. 1(c)]. The ideal current response is obtained from experimental current-voltage hysteresis curves [Fig. 1(a)] by subtracting the contribution of possible polarization currents due to ferroelectric switching from experimental hysteretic current-voltage curves [30]. Presented physical memristor model describes an ideal current response and has been tested on ideal hysteretic current-voltage curves of three different BFO thin films [29], which we obtained by subtracting the tiny contribution of polarization currents due to ferroelectric switching from experimental hysteretic current-voltage curves.

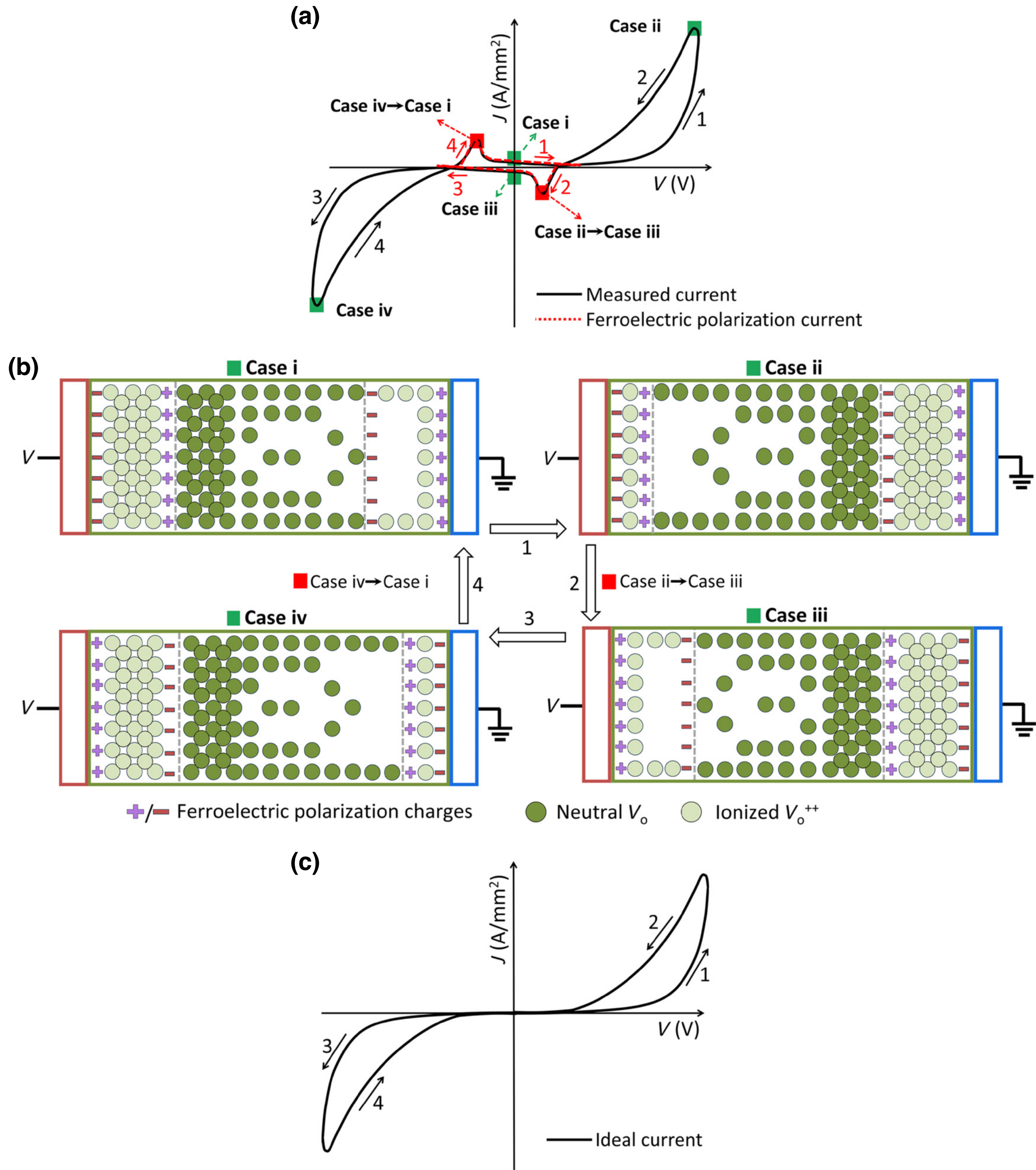

FIG. 1. (a) Schematics of a current density vs voltage (J-V) characteristic curve of a BFO memristor before ferroelectric correction (black-solid line) and superimposed schematics of a J-V characteristic curve of ferroelectric polarization current (red dotted line). (b) Distribution of ferroelectric polarization charge and of neutral and ionized oxygen vacancies in a BFO memristor in different cases i–iv, where the voltage is sourced to the top electrode (TE) (red-lined box) of BFO memristor with bottom electrode (BE) (green-lined box) being grounded: case i corresponds to the end of branch 4 and the start of branch 1 at zero applied bias $V = 0$ V. Case ii portrays the initiation of branch 2 and the termination of branch 1 with a maximum positive bias $V = +V_{\mathrm{max}}$ V. Case iii represents the commencement of branch 3 and the end of branch 2 at zero bias $V = 0$ V. Case iv depicts the onset of branch 4 and the end of branch 3 under maximum negative bias $V = -V_{\mathrm{max}}$ V. Distribution of polarization charges (+/−) and neutral oxygen vacancies ● (V_o), along with ionized oxygen vacancies ● (V_o^{+}, V_o^{++}), is depicted from case i to case iv [green squares in (**a**)]. The extension of the depletion layer of the TE and of the BE with ionized oxygen vacancies and the width of the undepleted layer with neutral oxygen vacancies is not to be scaled. The boundary of the depletion region below the TE and the boundary of the depletion region below the BE is marked by dotted gray lines. There are only the ferroelectric polarization charges in the depletion region. The ferroelectric switching is indicated by a polarity change of polarization charges. The positive polarization charges (+) and negative polarization charges (−) are flipped when going from case iv to case i [red triangles on branch 4 in (**a**)] and when going from case ii to case iii [red triangles on branch 2 in (a)]. (c) Schematics of an ideal J-V characteristic curve of a BFO memristor after ferroelectric correction (black-solid line). In this work, we present a physical model that describes ideal J-V curves after ferroelectric correction [solid line in (c)].

First, we analyze the change of the internal-state variables of BFO thin films with ideal current-voltage (I-V) characteristic curves under the electric field in the two write branches and relate it with the redistribution of oxygen vacancies in BFO memristors. Here, the current density J, $J = I/A$, with A being the area of the top electrode (TE) of BFO memristors is introduced, because that way extracted internal-state parameters are independent of the area of the TE. We show experimental current density–voltage curves in Fig. 1(a) and ideal current density–voltage curves in Fig. 1(c). The current I flows when the voltage V is ramped. We use ideal J-V hysteresis loops to extract the internal-state variables based on the simulation. We also present the unique aspects of oxygen vacancy drift in BFO memristor interface switching with the metallic conducting TE and the metallic conducting bottom electrode (BE), the TE and BE form a Schottky contact on the BFO thin film where they are attached. The extension of the depletion layer is indicated with a gray scattered line in Fig. 1(b). Notably, the ideal J-V curve is divided into four branches: branch 1 and branch 3 act as write branches, allowing modification to the internal state of the memristor, while branch 2 and branch 4 serve as read branches for retrieving the internal state, which have been written in branch 1 and branch 3, respectively. This partitioning is essential in comprehending the underlying operational principles of the BFO memristor. Accompanying the J-V curve, visualization of the distribution of mobile oxygen vacancies (V_o, V_o^+, V_o^{++}) in these different branches under various biases is explicitly depicted in Fig. 1(b). In particular, the figure portrays neutral oxygen vacancies (V_o) in the undepleted region and ionized oxygen vacancies in the depletion layer (V_o^+, V_o^{++}). Oxygen vacancies drift only in an electric field in branch 1 and branch 3. They drift in the direction of the electric field and are continuously redistributed after a threshold electric field strength. The final distribution of ionized oxygen vacancies depends on the voltage vs time ramping profile ($v = v(t)$) in branches 1 and 3. If the internal-state parameter at the beginning of a write branch is the same, then always the same memristance curve (flux charge) will be recorded for the same memristor. It does not matter how a given distribution of ionized oxygen vacancies is reached.

In our study, we investigate four distinct current-voltage branches 1-4. The four I-V branches differ with respect to the distributions of polarization charges and oxygen vacancies in BFO memristors. The analysis yields internal-state variables of BFO memristors in the four I-V branches 1-4. Armed with these insights into the internal-state variables, it will become feasible to design and develop electronic circuits with BFO memristors that unify data processing and storage functionality in the same cell without data transfer [29], while also successfully suppressing ferroelectric switching, thereby enhancing their applicability and performance. In more insulating conventional BFO thin-film scenarios, the ferroelectric current predominantly manifests within the insulating region [28], particularly in the area defined as the depletion region. It typically occurs when there is an incremental increase in the potential applied across the ferroelectric material. Contrary to this established behavior, our observations reveal an intriguing anomaly: the insulating region in our investigation is synonymous with the depletion region at the TE and BE, which form a Schottky contact. Given that the potential within this region is inversely related to the applied potential, the ferroelectric current is found to emerge as the applied potential diminishes [22]. This unexpected phenomenon presents another aspect of ferroelectric current behavior, opening an alternative dimension in our understanding of the underlying mechanics and may carry substantial implications for the design and operation of multiferroic memristors with interface switching where ferroelectric switching and its contribution to the current-voltage characteristics need to be suppressed, e.g., by random alignment of ferroelectric polarization in polycrystalline multiferroic memristors [31]. The multifaceted insights provided by Fig. 1 serve as a vital framework for future exploration and application in the field of memristor technology, as well as in the realm of multiferroic materials and oxygen vacancies drifting under the electric field in the write operation.

II. MODELING

From now on we use area independent internal-state variables, which are extracted from the current density J vs voltage curves. When examining the relationship between current density–voltage (J-V) characteristics of BFO memristors, we denote the layer structure of BFO memristor as TE/BFO/BE, with TE representing the top electrode, BFO representing the BFO layer, and BE representing the bottom electrode. Both junctions, the top electrode junction (TE/BFO) and the bottom electrode junction (BFO/BE) function as Schottky barriers (Fig. 1). Schottky barriers (Fig. 2) play an instrumental role in the electronic properties of metal-semiconductor devices. In Fig. 2, we specify the TE material as Au and the BE material as Pt/Ti. Specifically, in the TE/BFO/BE heterostructure, potential barriers emerge at the interfaces between the gold (Au) top electrode and the n-type semiconductor BFO, as well as between BFO and the Pt/Ti bottom electrode. When a metal, like Au with a work function of $\Phi_{\mathrm{Au}} = 5.15$ eV [32], or Pt with a work function of $\Phi_{\mathrm{Pt}} = 5.65$ eV [33], contacts the n-type semiconductor BFO with $\chi_{\mathrm{BFO}} = 3.3$ eV [34], electron migration occurs from the semiconductor to the metal until equilibrium is reached through Fermi-level alignment. The oxygen vacancies are redistributed in the two full-write branches of the hysteretic current-voltage curves of BFO memristors. It is worthwhile to note that the alignment of the

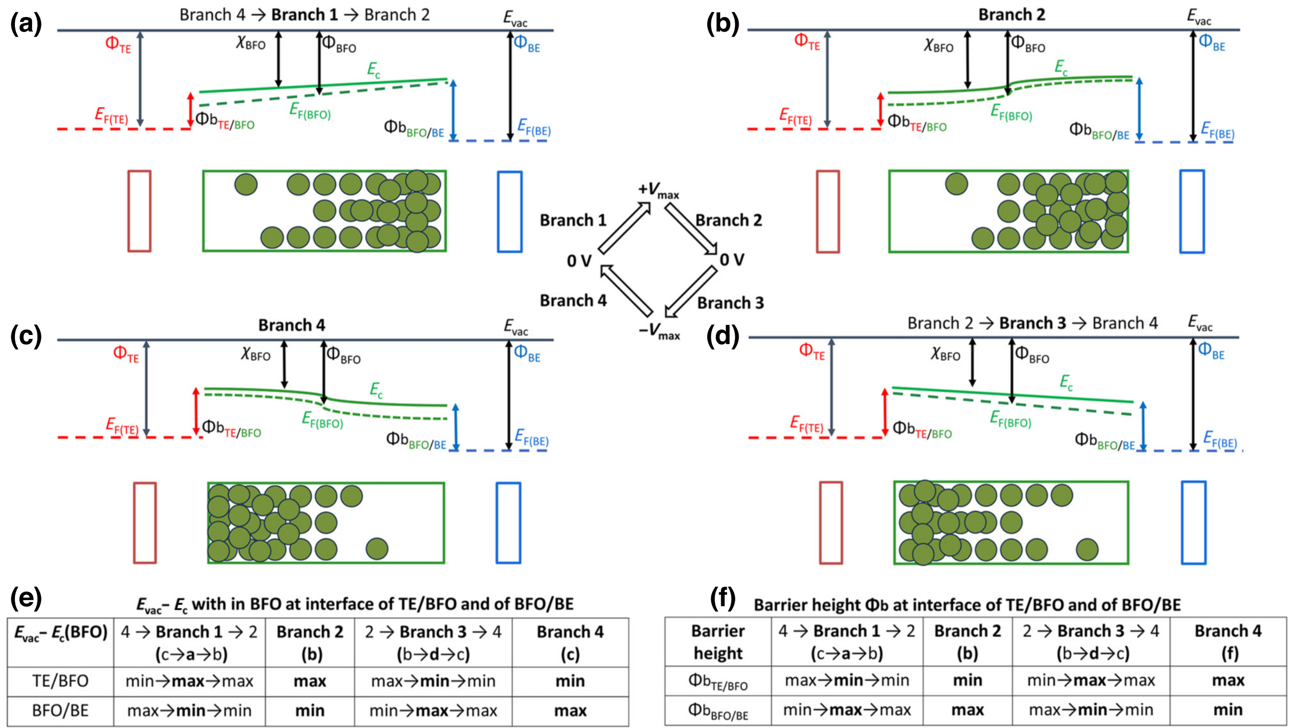

$E_{vac}-E_c$(BFO)	4 → **Branch 1** → 2 (c→**a**→b)	**Branch 2** (**b**)	2 → **Branch 3** → 4 (b→**d**→c)	**Branch 4** (**c**)
TE/BFO	min→**max**→max	**max**	max→**min**→min	**min**
BFO/BE	max→**min**→min	**min**	min→**max**→max	**max**

Barrier height	4 → **Branch 1** → 2 (c→**a**→b)	**Branch 2** (**b**)	2 → **Branch 3** → 4 (b→**d**→c)	**Branch 4** (**f**)
$\Phi b_{TE/BFO}$	max→**min**→min	**min**	min→**max**→max	**max**
$\Phi b_{BFO/BE}$	min→**max**→max	**max**	max→**min**→min	**min**

FIG. 2. Energy-band diagrams and relevant parameters of studied TE/BFO/BE structure where the TE, BFO, and BE are not in contact. The quasi-Fermi-level in BFO (E_F (BFO)), the work functions of the TE (Φ_{TE}) and BE (Φ_{BE}), and the position-dependent conduction-band minimum of BFO (E_C) are depicted with respect to the vacuum level (E_{vac}) in (a) An intermediate state in branch 1, (b) entire branch 2, (c) an intermediate state in branch 3, and (d) entire branch 4. The susceptibility of BFO χ_{BFO} is the difference between E_{vac} and E_C. Work functions and Fermi-level positions for the TE and BE are given as Φ_{TE} and E_F(TE), and Φ_{BE} and $E_F(BE)$, respectively. The barrier heights at the TE/BFO and BFO/BE interfaces are denoted as $\Phi b_{TE/BFO}$ and $\Phi b_{BFO/BE}$, respectively. The color scheme is TE (red) for the top electrode, BFO (green) for the n-type semiconductor, and BE (blue) for the bottom electrode. Listed are (e) the variation of the energy difference $E_{vac} - E_C$ within BFO and (f) the barrier height Φ_b at the TE/BFO interface and at the BFO/BE interface in dependence on the distribution of oxygen vacancies in branch 4 → branch 1 → branch 2, in branch 2, in branch 2 → branch 3 → branch 4, and in branch 4 by oxygen-vacancy concentration.

quasi-Fermi-level E_F and of the conduction-band minimum E_C depends on the distribution of free carriers and of oxygen vacancies, respectively. The dependence of the alignment of the conduction-band minimum E_C has been related with the distribution of the oxygen vacancies and the partial density of states of oxygen vacancies around the conduction-band minimum of BFO [35]. Because of reconfigured alignment of E_F and of E_C, it is expected that also the internal-state variables of the BFO memristor depend on the oxygen-vacancy distribution. In the presented Fig. 2, the intricate energy-band dynamics of a TE/BFO/BE heterostructure are meticulously showcased. Initial sections (a) to (d) provide comprehensive band diagrams depicting the transition and evolution of electronic states across different branches. Subsequently, (e) and (f) sections offer insights into the influence of oxygen-vacancy concentration on the energy difference within the BFO at the interfaces and the barrier-height parameters. This visualization is paramount in comprehending the correlation between susceptibility of BFO, work functions, Fermi levels, and barrier heights. The color coding further simplifies the understanding, wherein the top electrode (TE), the n-type semiconductor (BFO), and the bottom electrode (BE) are represented in shades of red, green, and blue, respectively. The figure's comprehensive representation is pivotal for grasping the advanced principles and nuances of TE/BFO/BE heterostructures, presenting it as a cornerstone for researchers and experts in the domain.

The Schottky barrier's magnitude, Φb, is determined by the energy difference between the conduction-band minimum of BFO (E_C) and the metal's work function (Φ_{TE} or Φ_{BE}). Interestingly, the total density of states at the conduction-band minimum of BFO (E_C) is only determined by the partial density of states of oxygen and iron, and not by the partial density of states of bismuth [35]. Missing oxygen atoms will reduce the total density of states at the conduction-band minimum of BFO (E_C). Therefore, in comparison to stoichiometric BFO without oxygen vacancies, for stoichiometric BFO with oxygen vacancies, the conduction-band minimum is shifted upwards and increases on the energy scale with increasing concentration of oxygen vacancies. The electron affinity

is reduced correspondingly. Figures 2(a)–2(d) demonstrate the variation in the energy difference between the vacuum level ($E_{\rm vac}$) and the conduction-band minimum (E_C), as well as the energy difference between the conduction-band minimum (E_C) and the metal's Fermi level (E_F(TE) or E_F(BE)) for different oxygen-vacancy distributions (branches 1–4), respectively. Qualitative values for these energy differences provided in Fig. 2(e) shows the energy difference between $E_{\rm vac}$ and E_C, and in Fig. 2(f) presents the energy difference between E_C and E_F(TE) or E_F(BE). The barrier heights at the interfaces of the *Au* top electrode/BFO and BFO/Pt/Ti bottom electrode are denoted as Φ_b(TE/BFO) and Φ_b(BFO/BE), respectively. Because oxygen vacancies are intrinsic donors in BFO, when being redistributed they consequentially modify the alignment of the quasi-Fermi-level in *n*-BFO [Figs. 2(a)–2(d)]. Therefore, the energy difference between the conduction-band edge and the Fermi level in BFO, labeled as $E_C - E_F$, is regulated by the oxygen-vacancy distribution. In essence, the Schottky barriers at the Au/BFO and BFO/Pt/Ti interfaces significantly impact the electronic properties of the heterostructure. Their heights are not only contingent upon the materials' work functions but are also affected by internal factors like the oxygen-vacancy distribution and the donor-quasi-Fermi-level concentrations in BFO. Comprehensive understanding of these potential barriers is pivotal for predicting and enhancing the performance of devices stemming from such TE/BFO/BE layer structures.

Figure 3(a) shows an example a linear voltage-time profile. The voltage-time profile determines the dynamics of internal parameter changes in the two full-write branches. However, it does not influence the internal parameters in the two full-read branches with their unique relation between applied voltage and applied current, which does not depend on the charge flown and the history of the voltage during read operation. Applied voltage sweep is classified into four current-density branches, 1 (branch 1, 0 to $+V_{\rm max}$), 2 (branch 2, $+V_{\rm max}$ to 0), 3 (branch 3, 0 to $-V_{\rm max}$) and 4 (branch 4, $-V_{\rm max}$ to 0). The corresponding equivalent circuits are shown in Fig. 3(b) and used to model measured current density–voltage curves of three BFO memristors (Fig. 2 in Ref. [29]).

The corresponding equivalent circuits are shown in Fig. 3(b) and used to model measured current density–voltage curves of three BFO memristors (Fig. 2 in Ref. [29]). If, for a given depletion layer, the leakage resistance $R_s \times A$ is very large, the leakage resistance can be neglected in the analysis of the corresponding Schottky barrier. Current flow over the leakage resistance $R_s \times A$ in the depletion layer of the top electrode [branch 2 in Fig. 3(b)] or over the leakage resistance $R_s \times A$ in the depletion layer of the bottom electrode [branch 4 in Fig. 3(b)] can be neglected if the concentration of oxygen vacancies is small. The extracted leakage resistance $R_s \times A$ in the depletion layer with large concentration of oxygen vacancies, i.e., in the depletion layer of the bottom electrode [branch 2 in Fig. 3(b)] and in the depletion layer of the top electrode [branch 4 in Fig. 3(b)] are listed in Table I and range between a few to hundreds of kΩ mm^2. Also, the Schottky barrier depends on the concentration of oxygen vacancies [36,37]. The prominent physical parameters describing the Schottky barriers are the reverse saturation current density (J_s) and the ideality factor (n). These parameters are integrated into the Schottky-barrier equation, $J_s \propto e^{-(\phi_B/k_BT)}$, as follows:

$$V_i = n\frac{k_BT}{q}\ln\left(\frac{J}{J_s}+1\right), \tag{1}$$

where ϕ_B, J, J_s, q, V_i, n, k_B, and T are barrier potential, current density, reverse saturation current density, the charge of an electron, voltage drop across the barrier, ideality factor, Boltzmann constant, and temperature. The reverse saturation current density (J_s) provides insight into the minority carrier activities, while the ideality factor (n) quantifies the divergence of the Schottky diode's real behavior from the ideal Schottky diode.

In the present study, we also address the influence of the position-dependent quasi-Fermi-energy E_F in the *n*-type

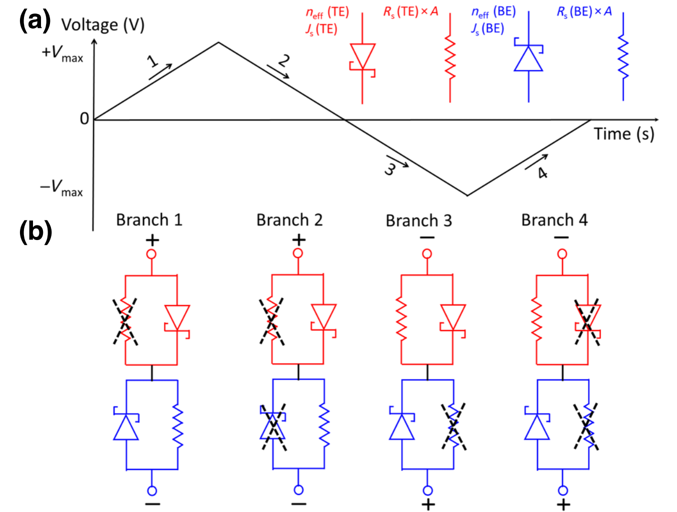

FIG. 3. Illustration of the linear voltage sweep and its corresponding equivalent circuit for the four distinct branches: branch 1 (0 V to $+V_{\rm max}$), branch 2 ($+V_{\rm max}$ to 0 V), branch 3 (0 V to $-V_{\rm max}$), and branch 4 ($-V_{\rm max}$ to 0 V). The equivalent circuit includes a description of two Schottky diodes with ideality factor ($n_{\rm eff}$) and reverse saturation current (J_s), along with a parallel leakage resistor (R_s). The TE/BFO and BFO/BE include the interface between BFO and the top electrode and between BFO and the bottom electrode, respectively. Black crossed-over lines within the diagram represent an insignificant circuit element for the specific branch under consideration. For example, the resistor in the connection TE/BFO is an insignificant circuit element in branch 1.

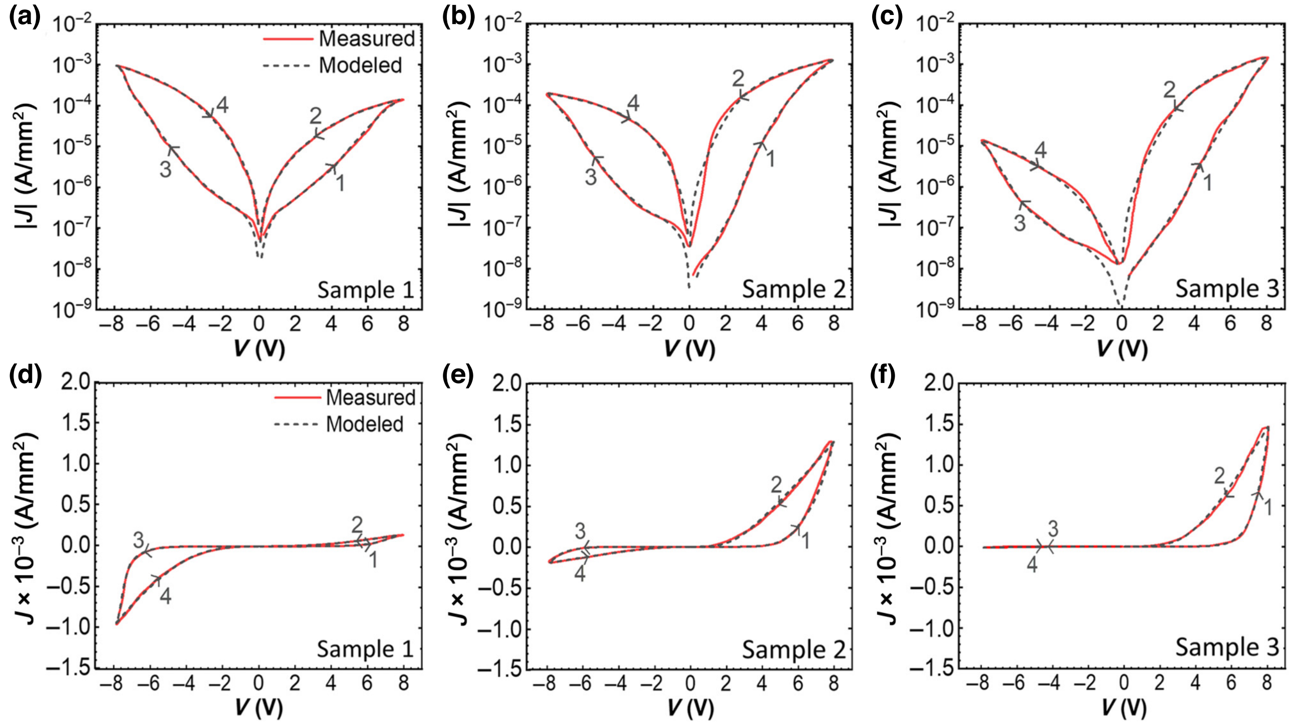

FIG. 4. Measured (red solid lines) and modeled (gray dashed lines) J-V characteristics shown in solid red lines of samples 1–3 from You *et al*. [29] where (a),(d) are sample 1, (b),(e) are sample 2, and (c),(f) are sample 3. J in (a)–(c) is in log scale and (d)–(f) is in linear scale. Switching directions of the samples are 1 (branch 1) → 2 (branch 2) → 3 (branch 3) → 4 (branch 4). (1, 3) and (2, 4) correspond to WRITE and READ branches, respectively.

BFO layer as demonstrated in the energy-band diagrams of Fig. 2, on the ideality factor n. It has been observed that n is contingent upon the recombination mechanisms and remains constant provided that the energy difference $E_C - E_F$ between the conduction-band minimum and the donor quasi-Fermi-energy within the BFO remains uniform throughout. However, as the energy diagrams in Fig. 2 parts (a) and (d) indicate, the presence of oxygen-vacancy drift introduces variability in $E_C - E_F$ at the interface of the TE/BFO/BE layer structure. This variation and also the variation of $E_{F(\mathrm{BFO})}$ in (b) and (c) necessitates a revision of the conventional ideality factor n to incorporate a dependency on the applied voltage, as the band-alignment changes dynamically fluctuate due to the dynamic drift of oxygen vacancies. Consequently, a modification to the ideality factor is proposed as a function of voltage, allowing for a more nuanced understanding of the Schottky-barrier behavior in the presence of nonuniform oxygen-vacancy distribution in the BFO layer and resulting nonuniform alignment of the donor-quasi-Fermi-level $E_{F(\mathrm{BFO})}$ (Fig. 2).

Instead of relating the ideality factor with the total applied voltage across the TE/BFO/BE structure, we introduce a current-density-dependent effective ideality factor, denoted as n_{eff}. This effective ideality factor accounts for the voltage drop across the specific contact under investigation. The relationship between the effective ideality factor, voltage drop across the barrier V_i, and current density J is given as follows:

$$n_{\mathrm{eff}} = n + (k \times V_i), \tag{2a}$$

where

$$n_{\mathrm{eff}} = n\left(1 + k\frac{k_B T}{q}\ln\left(\frac{J}{J_s} + 1\right)\right). \tag{2b}$$

Here, n is the conventional ideality factor from Eq. (1) and k (V^{-1}) is the proportionality constant. This reformulation offers a more targeted description of the device behavior, thereby enhancing the precision of the modeling and analysis specific to the contact configuration of interest. This approach paves the way for more accurate simulations and optimizations in various applications where the understanding of contact-specific behavior is crucial.

The TE/BFO junction is modeled as a forward-biased Schottky diode (FB), and the BFO/BE junction as a reverse-biased Schottky diode (RB), under conditions where the TE is positively biased and the BE is grounded (Fig. 3(b), branch 1 and branch 2). Conversely, when the TE is negatively biased and the BE is grounded, the TE/BFO junction is represented by a reverse-biased Schottky diode and the BFO/BE junction by a forward-biased Schottky diode (Fig. 3(b), branch 3 and branch 4).

Figure 4 shows double hysteresis switching characteristics of BFO memristor samples. The measured I-V data was taken from You *et al*. [29]. BFO memristor shows an interface switching, the physical model parameters presented do not depend on the area of TE and BE. Therefore, we took the area ($A = 4.53 \times 10^{-2}$ mm^2) of TE to model the current density J ($J = I/A$)–voltage (V) (red solid lines) characteristics and extract the physical model parameters in terms of J and RA. The branches corresponding to WRITE branches are 1 and 3 and READ branches are 2 and 4. WRITE branches are characterized by the application of high-voltage ramping and the memristor is switched from one stable state (high resistance state) to the other (low resistance state). By applying opposite polarity, the resistance state (low resistance state) of READ branches (2,4) can be reversed. A circuit model is developed with a set of Eq. (3) to simulate the effect of different distributions on the oxygen vacancies on the switching characteristics of BFO samples. In the following, we apply the presented simulation model to the current density–voltage hysteresis loops of three different BFO memristors. We call J-V curves with a hysteresis in the first and third J-V quadrant double J-V hysteresis. Those BFO memristors with double J-V hysteresis have been fabricated and investigated in a previous work [29] to demonstrate the reconfigurability of BFO memristors into the 16 Boolean logic gates. This was a key step towards data processing and storage in the same memristor device without data transfer. However, only now can one estimate the power consumption, speed, size, and cost of electronic circuits with BFO memristors using the presented physical model for electronic design automation simulations. The experimental current density–voltage hysteresis loops of the three different BFO memristors presented only in Ref. [29] contain small contributions from the ferroelectric polarization current density. We removed the ferroelectric polarization current density and obtained an ideal current density (Fig. 1). In the following, we report in detail on the extraction of the internal state variables [Fig. 3(b)] from the double J-V hysteresis with, branches 1-4 [Fig. 1(c)].

A comprehensive investigation of the double J-V hysteresis (Fig. 4) reveals two prominent resistance states, necessitating two distinct input signals for transition between them, as evidenced by the experimental data in Ref. [29]. The measured J-V characteristic curves of sample 1, sample 2, and sample 3 from You *et al*. [29] are depicted in Figs. 4(a)–4(c) on a logarithmic scale and in Figs. 4(d)–4(f) on a linear scale, after the subtraction of ferroelectric current density if necessary. Actually, the ferroelectric contribution of sample 1 and sample 3 is negligible and only the J-V curve of sample 2 shows a contribution from the ferroelectric polarization current in the small voltage range. We provide an ideal current density–voltage (J-V) data set, derived from the data as initially reported in You *et al*. [29]. Branch labels, 1–4, have been included in both types of representations. The behavior of the memristor can be partitioned into two diodes, specifically, the forward-bias diode and the reverse-bias diode, which is expressed by the following equation:

All branches

$$n_{\mathrm{RB}}^{\mathrm{eff}} = \left(n_{\mathrm{RB}} + n_{\mathrm{RB}} k_{\mathrm{RB}} \frac{k_B T}{q} \ln\left(\frac{-J_{D_{\mathrm{RB}}}}{J_{s_{\mathrm{RB}}}[-J]} + 1\right)\right), \tag{3a}$$

$$J_{D_{\mathrm{RB}}} = J_{s_{\mathrm{RB}}}[J]\left(e^{\Delta} - 1\right), \quad \text{where } \Delta = \frac{-qV_{\mathrm{RB}}}{n_{\mathrm{RB}}^{\mathrm{eff}} k_B T}, \tag{3b}$$

$$n_{\mathrm{FB}}^{\mathrm{eff}} = \left(n_{\mathrm{FB}} + n_{\mathrm{FB}} k_{\mathrm{FB}} \frac{k_B T}{q} \ln\left(\frac{J}{J_{s_{\mathrm{FB}}}[J]} + 1\right)\right), \quad \text{and} \tag{3c}$$

$$V = n_{\mathrm{FB}}^{\mathrm{eff}} \frac{k_B T}{q} \ln\left(\frac{J}{J_{s_{\mathrm{FB}}}[J]} + 1\right) + (J - J_{D_{\mathrm{RB}}}[J]) \times R_{\mathrm{RB}}[J] \times A. \tag{3d}$$

In Eq. (3), we present a comprehensive mathematical description of the J-V characteristics of a memristor, modeled as a series combination of a forward-bias diode and a reversed-bias diode. The effective ideality factors for the reverse- and forward-biased diodes are represented by $n_{\mathrm{RB}}^{\mathrm{eff}}$ and $n_{\mathrm{FB}}^{\mathrm{eff}}$, respectively, as shown in Eqs. (3a) and (3c). These effective ideality factors incorporate both the original ideality factors (n_{RB} and n_{FB}), the proportionality factors (k_{RB} and k_{FB}), and the thermal voltage ($k_B T/q$), modified by the current density (J) and the saturation current densities ($J_{s_{\mathrm{RB}}}$ and $J_{s_{\mathrm{FB}}}$) of the respective diodes similar to Eq. (2b).

In Eq. (3b), the current density through the reverse-biased diode ($J_{D_{\mathrm{RB}}}$) is expressed as a function of the applied voltage across the reverse-biased diode (V_{RB}), the effective ideality factor ($n_{\mathrm{RB}}^{\mathrm{eff}}$), and the saturation current density ($J_{s_{\mathrm{RB}}}$).

Finally, the overall voltage (V) across the memristor is described in Eq. (3d) as a function of the current density (J), the effective ideality factor ($n_{\mathrm{FB}}^{\mathrm{eff}}$), the saturation current density ($J_{s_{\mathrm{FB}}}$), the current density through the reverse biased diode ($J_{D_{\mathrm{RB}}}$), the resistance of the reverse-biased diode (R_{RB}), and the area of the top electrode (A).

TABLE I. Physical model parameters of samples 1–3 in branches 1–4, detailing the characteristics between the TE/BFO and BFO/BE interfaces in forward-bias and reverse bias. Modeled parameters n and k are associated with the n_{eff} as described in Eq. (2). The current density (J), reverse saturation current (J_s), and $\partial \log(J_s)/\partial \log(J)$ is a proportionality constant are extracted from the modeled Eqs. (A1)–(A4) The leakage resistance (R_s) is multiplied with contact area ($A = 4.53 \times 10^{-2}$ mm^2). The extracted parameters do not depend on the contact area. This representation is useful for memristors with interface switching. Subscripts TE and BE are inserted for n, k, J_s, R_s, and $\partial \log(J_s)/\partial \log(J)$ to represent top-electrode and bottom-electrode parameters.

	TE/BFO (1 ↑ & 2 ↓ → TE:FB, 3 ↑ → TE:RB)				**BFO/BE** (1 ↑ & 2 ↓ → BE:RB)		**BFO/BE** (↑ 3 & 4 ↓ → BE:FB, 1 ↑ → BE:RB)				**TE/BFO** (3 ↑ & 4 ↓ → TE:RB)	
Branch	n_{TE}	k_{TE} V^{-1}	Js_{TE} nA/mm^2	$\frac{\partial \log(Js_{\mathrm{TE}})}{\partial \log(J)}$	$Rs_{\mathrm{BE}}.A$ kΩ mm^2	$\frac{\partial \log(Rs_{\mathrm{BE}})}{\partial \log(J)}$	n_{BE} V^{-1}	k_{BE}	Js_{BE} nA/mm^2	$\frac{\partial \log(Js_{\mathrm{BE}})}{\partial \log(J)}$	$Rs_{\mathrm{TE}}.A$ kΩ mm^2	$\frac{\partial \log(Rs_{\mathrm{TE}})}{\partial \log(J)}$
						Sample 1						
1 ↑	32.00	0.30	540.84	+0.45	21.34	−0.81	4.88	0.01	234.00	...	...	...
2 ↓	24.00	2.75	540.84	...	21.34	...	...	...	...	...	...	...
3 ↑	24.00	60.00	540.84	...	...	...	23.00	0.40	234.00	+0.40	2.58	−0.99
4 ↓	...	...	...	...	...	...	4.88	19.6	234.00	...	2.58	...
						Sample 2						
1 ↑	16.00	0.20	624.72	+0.65	3.64	−0.80	11.40	6500.00	206.62	...	...	...
2 ↓	15.80	0.33	624.72	...	3.64	...	...	...	...	...	...	...
3 ↑	15.80	4000.00	624.72	...	...	...	16.00	0.15	206.62	+0.20	25.55	−0.93
4 ↓	...	...	...	...	...	...	11.40	2.42	206.62	...	25.55	...
						Sample 3						
1 ↑	19.00	0.16	103.09	+0.30	2.17	−0.90	6.85	0.1	7.04	...	...	...
2 ↓	9.24	4.50	103.09	...	2.17	...	...	...	...	...	...	...
3 ↑	9.24	1200.00	103.09	...	...	...	19.00	3.30	7.04	+0.25	126.84	-1.10
4 ↓	...	...	...	...	...	...	6.85	18.10	7.04	...	126.84	...

Together, these equations provide a comprehensive mathematical framework with physical parameters for understanding and modeling the electrical characteristics of write and read states of memristors, represented as a series combination of forward and reverse-biased diodes.

(1) **Write branch 1 and 3:** The write branches are characterized by the redistribution of oxygen vacancies under applied write voltage. In write branch 1 oxygen vacancies are drifting from the TE to the BE. And in write branch 3, the oxygen vacancies are drifting from the BE to the TE. The redistribution of oxygen vacancies changes the alignment of the quasi-Fermi-level in BFO with respect to the conduction-band minimum and with that also the internal-state parameter of the barrier height at the TE/BFO and at the BFO/BE interface. The other changing internal parameters are n_{eff}, J_s, and R_s as a function of current density J in Eq. (3).

(2) **Read branch 2 and 4:** This voltage does not redistribute the oxygen vacancies as long as maximum amplitude of read voltage is not larger than the maximum voltage of previously applied write voltage. Distribution of oxygen vacancies will occur only if a voltage of opposite polarity in comparison to the previously applied write voltage is applied to the BFO memristor. This again corresponds to the voltage ramping in a write branch. The current density at any voltage is accurately described by the internal-state parameters, i.e., by the internal-state variables at the largest bias of branch 1 for branch 2 and by the internal-state variables at the largest bias of branch 3 for branch 4: J_s and R_s. However, the ideality factor $n_{\mathrm{FB}}^{\mathrm{eff}}$ here is dependent on the voltage drop across the forward-bias Schottky contact (Eq. (2)).

III. METHODS

The fitting procedures for branches 1–4, as delineated in Eq. (3), were executed using Python in distinct methodologies to optimize accuracy and efficiency. Read branch 2, defined in Eq. (3b), and read branch 4, as per Eq. (3d), were subject to an automated fitting process. This approach leveraged the `least_squares` function in Python, a robust optimization tool commonly employed in computational data analysis. The function iteratively minimized the residuals between the observed data and the model predictions, adjusting the parameters to best fit the empirical observations. Conversely, write branch 1 (Eq. 3a) and write branch 3 (Eq. 3c) necessitated an iterative manual fitting approach. Such a manual approach is particularly beneficial in cases where the model behavior is complex or nonlinear, as it permits a more tailored fit to the dataset.

IV. RESULTS

The interface switching in memristors is affected by the physical properties of the memristor material involved, and the relationships between the current density J and voltage V. The internal-state variables of the memristor are crucial to understand its behavior and to develop electronic circuits with memristors, e.g., AI accelerators. The presented equations in the appendix, Eqs. (A1)–(A4), and the parameters listed in Table I are related to the analysis of interface switching in three different BFO memristors.

Table I presents a comprehensive overview of the physical model parameters pertaining to the three BFO memristors (samples 1–3) as they relate to four operational branches ($1\uparrow$, $2\downarrow$, $3\uparrow$, $4\downarrow$). These branches represent the intricate interactions occurring at the interfaces of the TE/BFO and BFO/BE under varying bias conditions, encompassing both forward and reverse biases. It is worth highlighting that the parameters n and k employed in our modeling are intricately linked to the effective parameter n_{eff}, as elaborated in Eq. (2).

Specifically, within branches $1\uparrow$ and $2\downarrow$, the TE/BFO interface operates as a forward-bias diode, while the BFO/BE interface functions as a reverse-bias diode [refer to Eqs. (A1)–(A4)]. Conversely, in branches $3\uparrow$ and $4\downarrow$, this configuration is reversed, with the TE/BFO acting as RB and BFO/BE as FB diodes. In the context of branches $2\downarrow$ and $4\downarrow$, it is noteworthy that the parameters n, k, J_s, and R_s exhibit no discernible variation in response to applied voltage changes. These parameters remain constant, underscoring their stability in these specific operational conditions. In contrast, within branches $1\uparrow$ and $3\uparrow$, we observe that the parameters n, k, and J_s for the RB diode remain unchanged over small voltage ranges, typically below 2 V. Furthermore, above 2 V, any variation in these parameters with applied voltage is deemed negligible for our modeling purposes. Notably, the parameters n and k for the FB diode hold validity across all voltage ranges in these branches and remain unaltered by changes in applied voltage.

It is crucial to emphasize that the voltage-dependent parameters in these branches are J_s (FB) and R_s (RB). We observe that the logarithm of J_s is directly proportional to the logarithm of J, while the logarithm of R_s is directly proportional to the negative logarithm of J. The precise proportionality constants governing these relationships are meticulously documented in Table I, as $\partial \log(Js_{\mathrm{TE\ or\ BE}})/\partial \log(J)$ and $\partial \log(Rs_{\mathrm{TE\ or\ BE}})/\partial \log(J)$, respectively. For a given cycle of resistive switching (RS) in 2D memristors, which exhibit significant cycle-to-cycle (C2C) variability, Spetzler *et al.* [38] also determined a proportionality constant between $\log I_s$ and $\log I$ [38]. Given the negligible C2C variability in BFO memristors, all parameters in Table I, including the proportionality constant between $\log I_s$ and $\log I$, are applicable for all cycles of RS in BFO memristors. It is noteworthy that as voltage increases, the barrier height of the FB diode decreases (J_s increases), while the leakage resistance R_s of the RB diode decreases correspondingly. Consequently, there exists an inverse relationship between the leakage resistance R_s of the RB diode and the barrier height of the RB diode, with both parameters exhibiting voltage-dependent behaviors.

Furthermore, our investigation revealed intriguing insights into the behavior of these diodes as a function of voltage. The order of change in the resistance parameter, denoted as R_s, of the reverse-bias diode is directly correlated with the maximum electrical current (J) at both the maximum positive voltage, denoted as $+V_{\max}$, and the maximum negative voltage, denoted as $-V_{\max}$. This relationship can be exemplified by comparing our findings for samples 1, 2, and 3, as illustrated in Fig. 4 and documented in Table I. For instance, at $+V_{\max}$, we observed R_s values of 21.34 kΩ mm^2, 3.64 kΩ mm^2, and 2.17 kΩ mm^2 for samples 1, 2, and 3, respectively, while the corresponding maximum J values were 1.35×10^{-4} A/mm^2, 1.24×10^{-3} A/mm^2, and 1.46×10^{-3} A/mm^2. Similarly, at $-V_{\max}$, R_s values were 2.58 kΩ mm^2, 25.55 kΩ mm^2, and 126.84 kΩ mm^2 for the same samples 1, 2, and 3, respectively, with corresponding maximum absolute J values of 8.74×10^{-3} A/mm^2, 1.75×10^{-4} A/mm^2, and 1.38×10^{-5} A/mm^2.

Figure 5 shows the extracted parameters from Eqs. (A1)–(A4). The extracted parameters for TE and BE are shown in red and blue color, respectively. Figures 5(a)–5(c) show simulated voltage drop over sample (TE/BFO/BE), and over junctions (TE/BFO and BFO/BE) for current density J. The effective ideality factor parameter, denoted as n_{eff} (Eq. (2)) and J_s, at the interfaces of TE/BFO and BFO/BE during the transition between operational branches ($1\uparrow\rightarrow 2\downarrow\rightarrow 3\uparrow\rightarrow 4\downarrow\rightarrow 1\uparrow$), is depicted in Figs. 5(d)–5(f) and in Figs. 5(g)–5(i), respectively. The n_{eff} and J_s are parameters that influence one another as they belong to the same diode. Similarly, for reverse-bias diodes, the parameter R_s is represented by solid lines in Figs. 5(j)–5(l). It is useful to note that the dotted lines in the figure represent estimated variations in an unknown branch, and these estimates may not be perfectly accurate. J_s typically changes only above 2 V and R_s also generally changes above 1 V, signifying the influence of the oxygen vacancy drift only after a threshold has been reached. As illustrated in Figs. 5(g)–5(i), the saturation current density J_s exhibits a plateau beyond a certain high-voltage threshold, indicating a stabilization in its value despite further voltage increases. This behavior is in agreement with the intermediate stages presented in Fig. 2, where the ferroelectric diode barrier height ΦB has reached its minimum level, particularly at the BFO/BE interface in branch 3, and the TE/BFO interface in branch 1. These

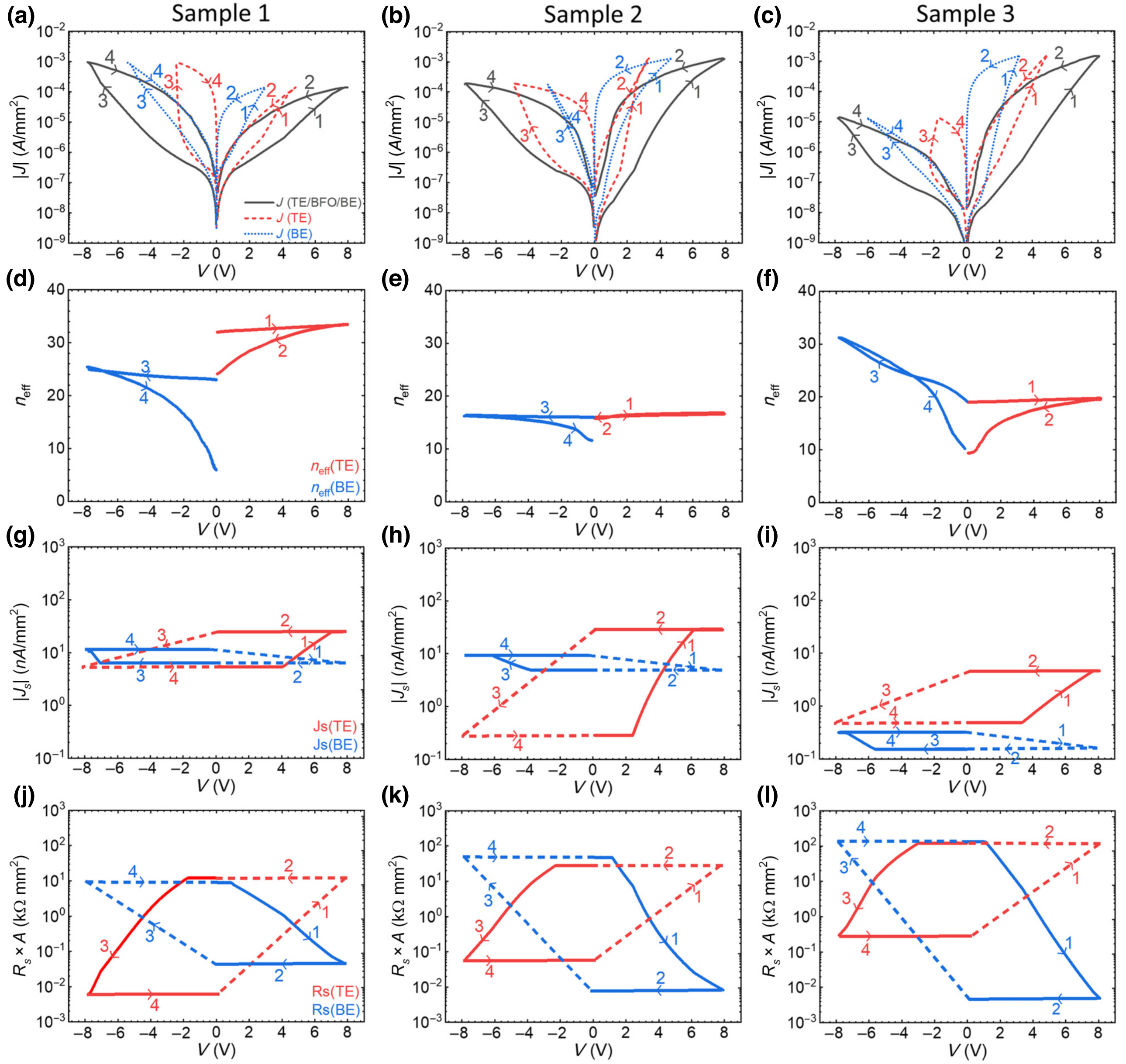

FIG. 5. (a)–(c) Modeled current density versus voltage (J-V) curves for the BFO memristor with two depletion regions (TE/BFO/BE), top electrode Schottky contact (TE/BFO), and the bottom electrode Schottky contact (BFO/BE). The modeled parameters (d)–(f) n_{eff}, (g)–(i) J_s, and (j)–(l) R_s are shown as a function of voltage for samples 1-3. The physical model parameters encompass the ideality factor (n_{eff}), the reverse saturation current (J_s), and the leakage resistance (R_s). Extracted parameters for TE and BE are shown in red and blue color, respectively.

insights are pivotal for simulating electronic circuits with interface-type memristors tailored for particular applications.

In conclusion, the analysis of Table I and Fig. 5 reveals crucial characteristics of the three distinct memristor samples across the four different operation branches 1–4. These insights are pivotal for optimizing memristor performance and can inform the design of memristors with specific characteristics tailored for particular applications.

V. CONCLUSIONS AND OUTLOOK

A physical memristor model of hysteretic current-voltage curves of the interface-type BFO memristor with hysteretic current-voltage curves has been developed. It assumes a change of internal-state variables in the two write branches due to dominating ion drift and no change of the internal-state variables in the two read branches where electron drift dominates. Primarily, the interface-type BFO memristor has been considered as a system

with two Schottky diodes in series. Every Schottky diode, the Schottky diode forming a depletion layer at the bottom electrode (BE) and the Schottky diode forming a depletion layer at the top electrode (TE), is described by an ideal Schottky barrier and a leakage resistance in parallel. The Schottky barrier and the leakage resistance of the reverse or forward Schottky diode at the TE and of the forward or reverse Schottky diode at the BE have been analyzed. Reported changes of barrier heights and leakage resistance correctly describe the current flow through the reverse or forward Schottky diode at the TE and the forward or reverse Schottky diode at the BE. Our findings rectify a previously misconstrued model of the Schottky barriers in interface-type, analog memristors, highlighting that both electrodes possess barriers, albeit one being dominantly shunted by the parallel leakage resistance. The redistribution of oxygen vacancies in the $n - \mathrm{BiFeO_3}$ (BFO) layer and its effect on the position-dependent band alignment of the conduction-band minimum and of the quasi-Fermi-level in BFO have been meticulously analyzed. It is the difference between E_C and E_F at the TE/BFO interface that influences the barrier height of the Schottky barrier at the TE and it is the difference between E_C and E_F at the BFO/BE interface that influences the barrier height of the Schottky barrier at the BE. A redistribution of oxygen vacancies will occur only and affect E_C and E_F and leakage resistance in the write branches 1 and 3. Our analysis has shed light on the correct dependence of Schottky-barrier height on the branch type being either write branch 1 and branch 3 or read branch 2 and branch 4. This marks a significant stride towards a physical memristor model describing the internal-state variables at every point of the hysteretic current-voltage curves of interface-type, analog memristors.

The insights garnered from the presented study not only contribute to the burgeoning literature on memristor technology, but also pave a promising avenue for the use of such interface-type, analog, and nonlinear memristors in electronic circuits for AI accelerators. Using the presented physical memristor model for electronic design automation simulations, the power consumption, speed, size, and cost of the electronic circuit can be estimated and compared with standard CMOS solutions.

ACKNOWLEDGMENTS

We wish to thank the Bundesagentur für Bildung und Forschung for financial support (BMBF project ForMikro—Grant No. ERMI 16ES1119).

APPENDIX A: *J-V* CHARACTERISTIC EQUATION FOR ALL BRANCHES

In Eqs. (A1)–(A4), we present a detailed mathematical framework for different branches of a memristor's J-V characteristics. Each branch corresponds to a different operational state of the memristor: write or read, as indicated by the up arrow (↑) for write branches and down arrow (↓) for read branches, and each branch has a unique set of parameters.

For branch 1 (Eq. (A1)), the equations describe the operation during a write operation (indicated by the superscript 1 ↑) where $n_{\mathrm{BE}}^{\mathrm{eff}}$ and $n_{\mathrm{TE}}^{\mathrm{eff}}$ are the effective ideality factors for the BE and TE diodes, respectively, and $J_{D_{\mathrm{BE}}}$ is the current density through the BE diode. V is expressed as a function of the current density J, effective ideality factors, and other parameters.

Branch 2 (Eq. (A2)) describes the operation during a read operation (indicated by the superscript 2 ↓), where $n_{\mathrm{eff}}^{\mathrm{TE}}$ is the effective ideality factor for the TE diode, and V is calculated based on the current density J, $n_{\mathrm{eff}}^{\mathrm{TE}}$, and other parameters. The following are equations for read (2 and 4) and write (1 and 3) branches:

Branch 1

$$n_{\mathrm{BE}}^{\mathrm{eff}} = \left(n_{\mathrm{BE}}^{1\uparrow} + n_{\mathrm{BE}}^{1\uparrow} k_{\mathrm{BE}}^{1\uparrow} \frac{k_B T}{q} \ln\left(\frac{-J_{D_{\mathrm{BE}}}}{J_{s_{\mathrm{BE}}}[-J]} + 1 \right) \right), \tag{A1a}$$

$$J_{D_{\mathrm{BE}}} = J_{s_{\mathrm{BE}}}[J] \left(e^{\Delta} - 1 \right), \quad \text{where } \Delta = \frac{-qV_{\mathrm{BE}}}{n_{\mathrm{BE}}^{\mathrm{eff}} k_B T}, \tag{A1b}$$

$$n_{\mathrm{TE}}^{\mathrm{eff}} = \left(n_{\mathrm{TE}}^{1\uparrow} + n_{\mathrm{TE}}^{1\uparrow} k_{\mathrm{TE}}^{1\uparrow} \frac{k_B T}{q} \ln\left(\frac{J}{J_{s_{\mathrm{TE}}}[J]} + 1 \right) \right), \quad \text{and} \tag{A1c}$$

$$V = n_{\mathrm{TE}}^{\mathrm{eff}} \times \frac{k_B T}{q} \ln\left(\frac{J}{J_{s_{\mathrm{TE}}}[J]} + 1 \right) + (J - J_{D_{\mathrm{BE}}}[J]) \times R_{\mathrm{BE}}[J] \times A. \tag{A1d}$$

Branch 2

$$n_{\rm eff}^{\rm TE} = \left(n_{\rm TE}^{2\downarrow} + n_{\rm TE}^{2\downarrow} k_{\rm TE}^{2\downarrow} \frac{k_B T}{q} \ln\left(\frac{J}{I_{s{\rm TE}}[+J_{\max}]} + 1\right)\right) \quad \text{and} \tag{A2a}$$

$$V = n_{\rm eff}^{\rm TE} \times \frac{k_B T}{q} \ln\left(\frac{J}{J_{s{\rm TE}}[+J_{\max}]} + 1\right) + J \times R_{\rm BE}[+J_{\max}] \times A. \tag{A2b}$$

Branch 3

$$n_{\rm TE}^{\rm eff} = \left(n_{\rm TE}^{3\uparrow} + n_{\rm TE}^{3\uparrow} k_{\rm TE}^{3\uparrow} \frac{k_B T}{q} \ln\left(\frac{-J_{D{\rm TE}}}{J_{s{\rm TE}}[J]} + 1\right)\right), \tag{A3a}$$

$$J_{D{\rm TE}} = J_{s{\rm TE}}[J]\left(e^{\Delta} - 1\right), \quad \text{where } \Delta = \frac{-qV_{\rm TE}}{n_{\rm TE}^{\rm eff} k_B T}, \tag{A3b}$$

$$n_{\rm BE}^{\rm eff} = \left(n_{\rm BE}^{3\uparrow} + n_{\rm BE}^{3\uparrow} k_{\rm BE}^{3\uparrow} \frac{k_B T}{q} \ln\left(\frac{J}{J_{s{\rm BE}}[J]} + 1\right)\right) \quad \text{and} \tag{A3c}$$

$$V = n_{\rm BE}^{\rm eff} \times \frac{k_B T}{q} \ln\left(\frac{J}{J_{s{\rm BE}}[J]} + 1\right) + (J - J_{D{\rm TE}}[J]) \times R_{\rm TE}[J] \times A. \tag{A3d}$$

Branch 4

$$n_{\rm eff}^{\rm BE} = \left(n_{\rm BE}^{4\downarrow} + n_{\rm BE}^{4\downarrow} k_{\rm BE}^{4\downarrow} \frac{k_B T}{q} \ln\left(\frac{-J}{I_{s{\rm BE}}[-J_{\max}]} + 1\right)\right) \quad \text{and} \tag{A4a}$$

$$V = -n_{\rm eff}^{\rm BE} \times \frac{k_B T}{q} \ln\left(\frac{-J}{J_{s{\rm BE}}[-J_{\max}]} + 1\right) + J \times R_{\rm TE}[-J_{\max}] \times A. \tag{A4b}$$

For branch 3 (Eq. (A3)), similar to branch 1 but for a different segment of the write operation (indicated by the superscript 3 ↑), $n_{\rm TE}^{\rm eff}$ and $n_{\rm BE}^{\rm eff}$ are the effective ideality factors for the TE and BE diodes, respectively, and $J_{D_{\rm TE}}$ is the current density through the TE diode.

Finally, branch 4 (Eq. (A4)) corresponds to another read operation (indicated by the superscript 4 ↓), where $n_{\rm eff}^{\rm BE}$ is the effective ideality factor for the BE diode, and V is calculated based on the current density J, $n_{\rm eff}^{\rm BE}$, and other parameters.

Together, these equations describe the memristor's I-V characteristics for different operational states (write or read) and enable a detailed understanding and modeling of the memristor's behavior.

[1] R. Dhall and H. Agrawal, An improved energy efficient duty cycling algorithm for IoT based precision agriculture, Procedia Comput. Sci. **141**, 135 (2018). the 9th International Conference on Emerging Ubiquitous Systems and Pervasive Networks (EUSPN-2018) / The 8th International Conference on Current and Future Trends of Information and Communication Technologies in Healthcare (ICTH-2018) / Affiliated Workshops.

[2] J. A. Ansere, E. Gyamfi, Y. Li, H. Shin, O. A. Dobre, T. Hoang, and T. Q. Duong, Optimal computation resource allocation in energy-efficient edge IoT systems with deep reinforcement learning, IEEE Trans. Green Commun. Netw. **7**, 1 (2023).

[3] J. C. S. dos Anjos, J. L. G. Gross, K. J. Matteussi, G. V. González, V. R. Q. Leithardt, and C. F. R. Geyer, An algorithm to minimize energy consumption and elapsed time for IoT workloads in a hybrid architecture, Sensors **21**, 2914 (2021).

[4] T. Berzina, A. Smerieri, M. Bernabò, A. Pucci, G. Ruggeri, V. Erokhin, and M. P. Fontana, Optimization of an organic memristor as an adaptive memory element, J. Appl. Phys. **105**, 124515 (2009).

[5] M. Spagnolo, J. Morris, S. Piacentini, M. Antesberger, F. Massa, A. Crespi, F. Ceccarelli, R. Osellame, and P. Walther, Experimental photonic quantum memristor, Nat. Photonics **16**, 318 (2022).

[6] K. Aryana, J. T. Gaskins, J. Nag, D. A. Stewart, Z. Bai, S. Mukhopadhyay, J. C. Read, D. H. Olson, E. R. Hoglund, J. M. Howe, A. Giri, M. K. Grobis, and P. E. Hopkins, Interface controlled thermal resistances of ultra-thin chalcogenide-based phase change memory devices, Nat. Commun. **12**, 774 (2021).

[7] N. Du, N. Manjunath, Y. Li, S. Menzel, E. Linn, R. Waser, T. You, D. Bürger, I. Skorupa, D. Walczyk, C. Walczyk,

O. G. Schmidt, and H. Schmidt, Field-driven hopping transport of oxygen vacancies in memristive oxide switches with interface-mediated resistive switching, Phys. Rev. Appl. **10**, 054025 (2018).

[8] M. Kiani, N. Du, D. Bürger, I. Skorupa, R. Ecke, S. E. Schulz, and H. Schmidt, in *2019 26th IEEE International Conference on Electronics, Circuits and Systems (ICECS)* (IEEE, Genova, 2019), p. 682.

[9] C. E. Graves, C. Li, X. Sheng, D. Miller, J. Ignowski, L. Kiyama, and J. P. Strachan, In-memory computing with memristor content addressable memories for pattern matching, Adv. Mater. **32**, 2003437 (2020).

[10] C. Li, D. Belkin, Y. Li, P. Yan, M. Hu, N. Ge, H. Jiang, E. Montgomery, P. Lin, Z. Wang, J. P. Strachan, M. Barnell, Q. Wu, R. S. Williams, J. J. Yang, and Q. Xia, in *2018 IEEE International Memory Workshop (IMW)* (2018), p. 1.

[11] W. Xu, J. Wang, and X. Yan, Advances in memristor-based neural networks, Front. Nanotechnol. **3**, 645995 (2021).

[12] Z. Cao, B. Sun, G. Zhou, S. Mao, S. Zhu, J. Zhang, C. Ke, Y. Zhao, and J. Shao, Memristor-based neural networks: A bridge from device to artificial intelligence, Nanoscale Horiz. **8**, 716 (2023).

[13] C. Li, D. Belkin, Y. Li, P. Yan, M. Hu, N. Ge, H. Jiang, E. Montgomery, P. Lin, Z. Wang, W. Song, J. P. Strachan, M. Barnell, Q. Wu, R. S. Williams, J. J. Yang, and Q. Xia, Efficient and self-adaptive in-situ learning in multilayer memristor neural networks, Nat. Commun. **9**, 2385 (2018).

[14] D. Wang, J. Xu, D. Stathis, L. Zhang, F. Li, A. Lansner, A. Hemani, Y. Yang, P. Herman, and Z. Zou, Mapping the BCPNN learning rule to a memristor model, Front. Neurosci. **15**, 750458 (2021).

[15] N. Du, N. Manjunath, Y. Shuai, D. Bürger, I. Skorupa, R. Schüffny, C. Mayr, D. N. Basov, M. Di Ventra, O. G. Schmidt, and H. Schmidt, Novel implementation of memristive systems for data encryption and obfuscation, J. Appl. Phys. **115**, 124501 (2014).

[16] R. A. John, N. Shah, S. K. Vishwanath, S. E. Ng, B. Febriansyah, M. Jagadeeswararao, C.-H. Chang, A. Basu, and N. Mathews, Halide perovskite memristors as flexible and reconfigurable physical unclonable functions, Nat. Commun. **12**, 3681 (2021).

[17] Y. Wei, Z. Liu, D. Xu, L. Dong, G. Li, Y. Wang, F. Fan, X. Meng, and J. Song, Dielectric properties and ferroelectric resistive switching mechanism in the epitaxial (111) $BiFeO_3$ films, Ferroelectrics **613**, 97 (2023).

[18] F. Qin, Y. Zhang, H. W. Song, and S. Lee, Enhancing memristor fundamentals through instrumental characterization and understanding reliability issues, Mater. Adv. **4**, 1850 (2023).

[19] H. Schmidt, Prospects for memristors with hysteretic memristance as so-far missing core hardware element for transfer-less data computing and storage, J. Appl. Phys. **135**, 200902 (2024).

[20] T. You, N. Du, S. Slesazeck, T. Mikolajick, G. Li, D. Bürger, I. Skorupa, H. Stöcker, B. Abendroth, A. Beyer, K. Volz, O. G. Schmidt, and H. Schmidt, Bipolar electric-field enhanced trapping and detrapping of mobile donors in $BiFeO_3$ memristors, ACS Appl. Mater. Interfaces **6**, 19758 (2014).

[21] N. Du, Y. Shuai, W. Luo, C. Mayr, R. Schüffny, O. G. Schmidt, and H. Schmidt, Practical guide for validated memristance measurements, Rev. Sci. Instrum. **84**, 023903 (2013).

[22] A. Chen, W. Zhang, L. R. Dedon, D. Chen, F. Khatkhatay, J. L. MacManus-Driscoll, H. Wang, D. Yarotski, J. Chen, X. Gao, L. W. Martin, A. Roelofs, and Q. Jia, Couplings of polarization with interfacial deep trap and Schottky interface controlled ferroelectric memristive switching, Adv. Funct. Mater. **30**, 2000664 (2020).

[23] S. Yarragolla, N. Du, T. Hemke, X. Zhao, Z. Chen, I. Polian, and T. Mussenbrock, Physics inspired compact modelling of $BiFeO_3$ based memristors, Sci. Rep. **12**, 20490 (2022).

[24] L. Gao, Q. Ren, J. Sun, S.-T. Han, and Y. Zhou, Memristor modeling: challenges in theories, simulations, and device variability, J. Mater. Chem. C **9**, 16859 (2021).

[25] J. R. Teague, R. Gerson, and W. James, Dielectric hysteresis in single crystal $BiFeO_3$, Solid State Commun. **8**, 1073 (1970).

[26] P. Fischer, M. Polomska, I. Sosnowska, and M. Szymanski, Temperature dependence of the crystal and magnetic structures of $BiFeO_3$, J. Phys. C: Solid State Phys. **13**, 1931 (1980).

[27] K. Jang, M. Kobayashi, and T. Hiramoto, Role of gate current and polarization switching in sub-60 mV/decade steep subthreshold slope in metal–ferroelectric $HfZrO_2$–metal–insulator–Si FET, Jpn. J. Appl. Phys. **57**, 114202 (2018).

[28] Z. Wang, X. Yang, X. He, H. Xue, X. Wang, H. Dong, J. Zhu, W. Mao, X. Xu, and X. Li, Roles of oxygen vacancy and ferroelectric polarization in photovoltaic effects of $BiFeO_3$ based devices, Solid State Commun. **360**, 115042 (2023).

[29] T. You, Y. Shuai, W. Luo, N. Du, D. Bürger, I. Skorupa, R. Hübner, S. Henker, C. Mayr, R. Schüffny, T. Mikolajick, O. G. Schmidt, and H. Schmidt, Exploiting memristive $BiFeO_3$ bilayer structures for compact sequential logics, Adv. Funct. Mater. **24**, 3357 (2014).

[30] B. Sun, M. Xiao, G. Zhou, Z. Ren, Y. Zhou, and Y. Wu, Non–zero-crossing current-voltage hysteresis behavior in memristive system, Mater. Today Adv. **6**, 100056 (2020).

[31] S. Li and T. Birol, Suppressing the ferroelectric switching barrier in hybrid improper ferroelectrics, npj Comput. Mater. **6**, 168 (2020).

[32] J. W. Kim and A. Kim, Absolute work function measurement by using photoelectron spectroscopy, Curr. Appl. Phys. **31**, 52 (2021).

[33] B. Ofuonye, J. Lee, M. Yan, C. Sun, J.-M. Zuo, and I. Adesida, Electrical and microstructural properties of thermally annealed Ni/Au and Ni/Pt/Au Schottky contacts on AlGaN/GaN heterostructures, Semicond. Sci. Technol. **29**, 095005 (2014).

[34] S. J. Clark and J. Robertson, Band gap and Schottky barrier heights of multiferroic $BiFeO_3$, Appl. Phys. Lett. **90**, 132903 (2007).

[35] Materials Project, Materials data on [name of the material] by materials project (2024), https://legacy.materialsproject.org/materials/mp-24932/, accessed: [01.05.2024].

[36] G. Y. Yang, G. D. Lian, E. C. Dickey, C. A. Randall, D. E. Barber, P. Pinceloup, M. A. Henderson, R. A. Hill, J. J. Beeson, and D. J. Skamser, Oxygen nonstoichiometry and

dielectric evolution of $BaTiO_3$. Part II—insulation resistance degradation under applied dc bias, J. Appl. Phys. **96**, 7500 (2004).

[37] Y. Noguchi and M. Miyayama, in *Handbook of Advanced Dielectric, Piezoelectric and Ferroelectric Materials*, Woodhead Publishing Series in Electronic and Optical Materials, edited by Z.-G. Ye (Woodhead Publishing, Cambridge, 2008), p. 1006.

[38] B. Spetzler, D. Abdel, F. Schwierz, M. Ziegler, and P. Farrell, The role of vacancy dynamics in two-dimensional memristive devices, Adv. Electron. Mater. **10**, 2300635 (2024).